

Dynamical response of ultracold interacting fermion-boson mixtures: Fermion-hole vs polaron-hole excitations.

Stefan Maier,* Kai Ji,* and Andreas Komnik
*Institut für Theoretische Physik, Universität Heidelberg,
 Philosophenweg 19, D-69120 Heidelberg, Germany*
 (Dated: November 19, 2019)

We analyze the dynamical response of a ultracold binary gas mixture in presence of strong boson-fermion couplings. Mapping the problem onto that of the optical response of a metal/semiconductor electronic degrees of freedom to electromagnetic perturbation we calculate the corresponding linear response susceptibility in the non-perturbative regimes of strong boson-fermion coupling using diagrammatic resummation technique as well as quantum Monte Carlo simulations. Depending on the interaction strength and the details of the underlying bosonic spectra we find that energy absorption/emission can occur due to excitation of individual fermions as well as fully dressed polarons.

PACS numbers: 71.38.Fp, 78.20.Bh, 03.75.Mn, 67.85.De

I. INTRODUCTION

Ultracold gas mixtures of bosons and fermions, which arise very naturally in the sympathetic cooling processes, are very interesting quantum systems with physical properties very different from conventional quantum gases.^{1,2} In view of recent advances in the field of correlated ultracold gases it is very important to understand their dynamical properties, e. g. their response to an external dynamical scattering potential brought about by a change of trapping potential. If the bosonic subsystem is dominantly in the BEC phase the effective low-energy interaction with the fermionic subsystem is the coupling between the latter and the phonons (sound waves) of the former. From the mathematical point of view such a system is nothing but an electron-phonon coupled system best described by the Fröhlich Hamiltonian.³ In case of low fermion concentrations it describes individual impurities imbedded into a continuum of massless bosonic modes. Under such conditions the physics of the system is supposed to be very close to that of the classical polaron, taking place in semiconductors with strong electron-phonon interaction.⁴⁻⁶

There are, however, fundamental differences between the conventional (solid state) polarons and their BEC counterparts. The most obvious one is the different phonon spectrum of the bosonic subsystem as well as an explicit momentum dependence of the electron-phonon coupling.⁶ While these details do not alter the general picture of polaron static properties (there is still an effective mass generation and self-trapping), they could possibly alter the dynamical response, which reveals such important information as how the impurities interact with their surroundings.^{7,8} In this paper we would like to consider them in full detail and in different geometries with the special emphasis on strong coupling results thereby closing the gaps in the existing literature.

The paper is organized as follows. In the next section we formulate the problem and introduce all relevant quantities. Section III is devoted to the non-perturbative

approach inspired by the classical random phase approximation (RPA). We explain the details of the implementation and discuss the special features pertinent to ultracold gas realizations. In Section IV the calculation of the dynamical response function is accomplished using numerically exact quantum Monte Carlo simulation technique. Section V contains a discussion of results and offers several avenues of further progress.

II. THE MODEL AND OBSERVABLES

An effective low-energy Hamiltonian for a BEC-fermion mixture has the canonical Fröhlich form,^{3,6} which is written in terms of boson (described by the field operators $b_{\mathbf{k}}$) and fermion (denoted by $a_{\mathbf{q}}$) degrees of freedom,

$$H = \sum_{\mathbf{q}} E_{\mathbf{q}} a_{\mathbf{q}}^{\dagger} a_{\mathbf{q}} + \sum_{\mathbf{k}} \omega_{\mathbf{k}} b_{\mathbf{k}}^{\dagger} b_{\mathbf{k}} + \sum_{\mathbf{q}} \sum_{\mathbf{k} \neq 0} V_{\mathbf{k}} a_{\mathbf{q}+\mathbf{k}}^{\dagger} a_{\mathbf{q}} (b_{\mathbf{k}} + b_{-\mathbf{k}}^{\dagger}), \quad (1)$$

where the dispersion of the fermion is $E_{\mathbf{q}} = q^2/2m$,

$$\omega_{\mathbf{k}} = ck[1 + (\xi k)^2/2]^{1/2} \quad (2)$$

is the dispersion of the phonon mode and the coupling is given by $V_{\mathbf{k}} = \lambda[(\xi k)^2/((\xi k)^2 + 2)]^{1/4}$ with $\lambda = g_{\text{IB}} \sqrt{N_0}$. g_{IB} is the effective interaction strength between impurities and Bogoliubov excitations and can be adjusted by changing the particle density and/or the s-wave scattering length of collision processes of the impurity with the bosonic medium. ξ denotes the healing length of the condensate and is given by $\xi = 1/\sqrt{8\pi a_{\text{BB}} n_0}$ where a_{BB} is the boson-boson s-wave scattering length and n_0 is the condensate density.

One fundamental difference between the ‘classical’ semiconductor based electron-phonon coupled system and the one realized in ultracold mixtures is that the quantum gas system can be prepared in trapping potentials for fermions and bosons which might be of different

shape and dimensionality. For that reason we shall later consider systems with different $E_{\mathbf{q}}$ and $\omega_{\mathbf{k}}$. Changing the shape of the trapping potential for the impurity in space and time, for instance by acceleration with respect to the BEC, which rests in the laboratory reference frame one induces the rearrangement of particles. Another possible probing process is the Bragg spectroscopy.^{9–11} An appropriate response function to that is the autocorrelation of the particle current density. This picture directly corresponds to the conventional polaron, where the response function is charge current autocorrelation, which is related to the frequency-dependent or optical conductivity $\sigma(\omega)$.¹² In order to establish immediate parallels to the classical polaron problem we shall call the quantity in question optical conductivity as well.

In general the optical conductivity is a complex quantity. While the imaginary part describes attenuation of the excitations, the real part is the actual emission/absorption spectra. We shall concentrate on the latter. It can be shown that

$$\text{Re}[\sigma(\omega)] = -\text{Im}[\pi(\omega)/\omega], \quad (3)$$

where $\pi(\omega)$ is referred to as force-force correlation function, which is up to some frequency dependent prefactor proportional to the correlation function of the perturbation on the rhs of (1).¹³ The calculation is most convenient in the Matsubara representation, where we have

$$\begin{aligned} \pi(i\omega) &= \frac{e^2}{m^2(i\omega)^2 V} \sum_{\mathbf{q}, \mathbf{q}'} q_{\mu} q'_{\mu} \int_0^{\beta} d\tau e^{i\omega\tau} \\ &\times \langle T_{\tau} \rho(\mathbf{q}, \tau) \rho(\mathbf{q}', 0) \Phi(\mathbf{q}, \tau) \Phi(\mathbf{q}', 0) \rangle \end{aligned} \quad (4)$$

with the density operator

$$\rho(\mathbf{q}) = \frac{1}{V} \sum_{\mathbf{k}} a_{\mathbf{k}}^{\dagger} a_{\mathbf{k}+\mathbf{q}}, \quad (5)$$

and the generalized potential

$$\Phi(\mathbf{q}) = V_{\mathbf{q}} (b_{\mathbf{q}} + b_{-\mathbf{q}}^{\dagger}). \quad (6)$$

The subscript μ in the double sum indicates the spatial direction with respect to which the conductance is probed, that is $\mu \in \{x, y, z\}$. After the computation of $\pi(i\omega)$ one has to perform an analytic continuation and then extract the optical conductivity using the prescription (3).

Before proceeding with the actual calculation, a remark is in order. From the perspective of a solid-state physicist, the optical conductivity describes the experimental conditions quite well, that is probing a sample with optical or X-ray photons does not lead to a substantial momentum transfer ($\Delta\mathbf{p} \approx 0$). In case of the RF-spectroscopy in ultracold quantum gases, this is not necessarily the case. In order to use the abovementioned force-force correlation function, the absence of momentum transfer is essential. The Monte Carlo scheme discussed later, however, is quite more general and allows

for the consideration of an arbitrary momentum transfer. In this case, a more suitable observable is the real part of the fully momentum-dependent optical conductivity,¹⁴

$$\text{Re}[\sigma_{\mu\nu}(\mathbf{q}, \omega)] = -\frac{e^2}{\omega} \text{Im}[\Pi_{\mu\nu}(\mathbf{q}, \omega)], \quad (7)$$

where, again, the most convenient form for the current-current correlation function $\Pi(\mathbf{q}, \omega)$ is the Matsubara representation,

$$\Pi_{\mu\nu}(\mathbf{q}, \tau) = -\frac{1}{V} \langle T_{\tau} j_{\mu}^{\dagger}(\mathbf{q}, \tau) j_{\nu}(\mathbf{q}, 0) \rangle, \quad (8)$$

with the current densities

$$j(\mathbf{q}) = -\frac{1}{m\beta V} \sum_{\mathbf{k}} \left(\mathbf{k} + \frac{\mathbf{q}}{2} \right) a_{\mathbf{k}}^{\dagger} a_{\mathbf{k}+\mathbf{q}}. \quad (9)$$

In the analytic approach as well as in the Monte Carlo scheme we restrict ourselves to the case of one dimensional systems, hence skip the vector notation. Experimentally, this can be motivated by the use of quantum gases in reduced dimensions.

If not explicitly stated otherwise we use the polaronic units. Distances are measured in ξ , time in units of $m\xi^2/\hbar$ and energies in units of $\hbar^2/(m\xi^2)$.

III. RPA RESULTS FOR THE RESPONSE FUNCTION

Analytical approaches have been widely used in the investigation of the effects of electron-phonon interactions in metals and semiconductors (for the latest review, consult e. g. Ref. [15]). Very recently, due to formal similarities much effort has been made to adapt these methods to Bose-Fermi mixtures^{6,16–22}. Although the applicability and accuracy of these approximation schemes have in general to be questioned,²³ their simplicity allows for an easy way to get first insights into the complex nature of electron-phonon interaction. Especially when it comes to the interpretation of numerical data, such analytical models proved to be of much use and importance.

We begin our calculations with a simple perturbative treatment of the optical conductivity using the force-force correlation function. Mainly, we are interested in the effect of different energy-momentum relations ω_k and interaction potentials V_k . We are looking at the conventional Fröhlich model with an LO phonon (ω_k, V_k) = ($\Omega_0, \lambda/|k|$), the acoustic phonon model (ω_k, V_k) = ($|k|, \lambda/\sqrt{|k|}$), the small momenta BEC-polaron model²⁴ (ω_k, V_k) = ($c|k|, \lambda\sqrt{|k|}$) and, of course, the full BEC-polaron model as presented in the previous section.

The leading order contribution to the conductivity is found by replacing the expectation value with respect to the full Hamiltonian in Eq. (4) by an expectation value

for the non-interacting system,¹²

$$\pi(i\omega) = -\frac{e^2}{m^2(i\omega)^2 V} \sum_q q^2 V_q^2 \times \frac{1}{\beta} \sum_{i\nu} \mathcal{D}^{(0)}(q, i\nu) [\chi^{(0)}(q, i\omega + i\nu) - \chi^{(0)}(q, i\nu)], \quad (10)$$

where $\mathcal{D}^{(0)}(q, i\nu)$ is the Green's function of the phonon mode and $\chi(q, i\omega + i\nu)$ is the density-density correlation function (polarization loop) defined as

$$\chi^{(0)}(q, \tau) = -\langle T_\tau \rho(q, \tau) \rho(-q, 0) \rangle_0. \quad (11)$$

The corresponding Feynman diagram is depicted in Fig. 1. The calculation of the free phonon propagator

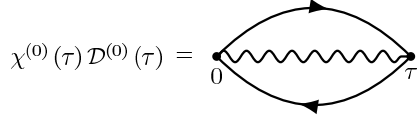


FIG. 1. Leading order contribution to the conductance. The wiggly line represents the free phonon propagator and the solid lines denotes the free Green functions of the impurities

as well as the free polarization loop is straightforward, one obtains,

$$\mathcal{D}^{(0)}(q, i\nu) = \frac{1}{i\nu - \omega_q} - \frac{1}{i\nu + \omega_q} \quad (12)$$

and

$$\chi^{(0)}(q, i\nu) = \frac{1}{V} \sum_k \frac{n_F(\epsilon_k) - n_F(\epsilon_{k+q})}{i\nu + \epsilon_k - \epsilon_{k+q}} \quad (13)$$

where n_F denotes the Fermi-Dirac distribution function and $\epsilon_k = E_k - \mu$ with the chemical potential μ . The remaining Matsubara summation and the analytical continuation $i\omega_n \rightarrow \omega + i0^+$ are straightforward. One obtains for the conductance,

$$\text{Re}[\sigma(\omega)] = \frac{e^2}{m\omega^3} \int \frac{dq}{4\pi} \sum_{r,s=\pm} s [n_B(\omega_q) - n_B(\omega_q + rs\omega)] \times |q| V_q^2 n_F(\epsilon_{\tilde{q}}) \Big|_{\tilde{q}=\frac{m}{q}(\omega+rs\omega_q)-\frac{sq}{2}} \quad (14)$$

where n_B is the Bose-Einstein distribution function. In Fig. 2 the conductivity is depicted for the above-mentioned models for several chemical potentials. The Fröhlich model shows the well-known threshold behaviour (i.e. $\sigma \approx 0$ for $\omega < \Omega_0$). At finite temperature, each considered model shows a divergent tendency for small frequencies. This is due to the combination of the coefficient $1/\omega^3$ and the factor consisting of Bose-Einstein distribution functions. In the limit $\omega \rightarrow 0$ one usually expects to obtain the DC conductivity in the case of the ‘canonical’ polaron system. This feature is also referred to as the Drude peak. It is the static response to

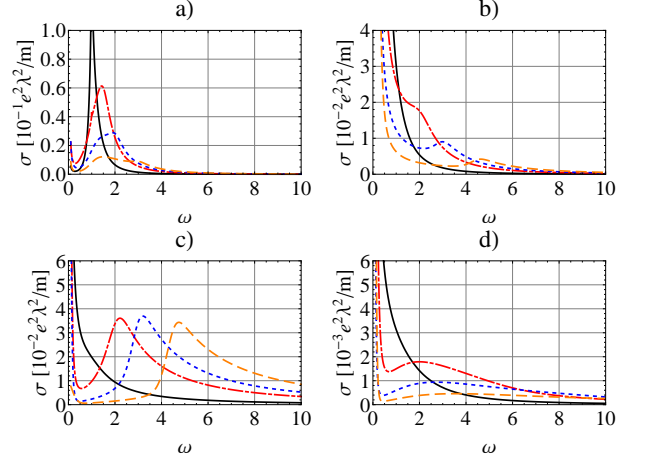


FIG. 2. (Color online) Real part of the conductivity for the discussed models and several chemical potentials. Panel a) the LO model ($\Omega_0 = 1$), b) the acoustic phonon model, c) the small momenta BEC polaron model and d) the BEC polaron model. The temperature is fixed to $\beta = 10$ and the chemical potential is varied: $\mu = 0, 0.5, 1, 2$ (black solid, red dot-dashed, blue dashed and orange long-dashed line).

a constant electric field and might indeed be rather large as compared to the rest of the spectrum. In the BEC case this Drude peak is directly related to the mobility of the impurity. In order to obtain the purely dynamical response it is sensible to subtract the $\omega = 0$ result. Interestingly, for temperatures approaching zero where the n_B can be approximated by $n_B(\omega) = -\Theta(-\omega)$ this tendency is strongly suppressed (see Fig. 3).

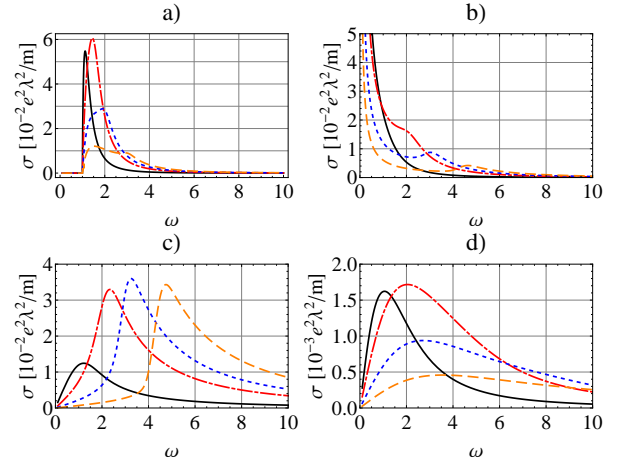


FIG. 3. (Color online) Real part of the conductivity for the discussed models and several chemical potentials. Same conventions as in Fig. 2 except for the approximation $n_B(\omega) \approx -\Theta(-\omega)$.

The effect of increasing chemical potential is a shift

of the peak-like structure towards higher frequencies. In the LO model an additional feature can be observed: a double peak structure emerges (one peak at $\omega \approx \Omega_0$ and another one at $\omega \approx \Omega_0 + \mu$). For non-trivial energy-momentum relations ω_q this feature is washed out. This double-peak structure has a natural explanation. The optical response measures how easy it is to excite an electron-hole pair. The existence of the first threshold is trivial: if there is not enough energy to overcome Ω_0 than the response is suppressed. With growing ω one has to ‘dig’ deeper into the Fermi sea. The maximal energy for the electron-hole pair is then equal to the band depth, which in the present case is equal to μ .

In order to go beyond the perturbative analysis, several field theoretical approximation schemes are available. We have chosen to use the random-phase approximation, which is good for systems with efficient screening. Usually this happens only in systems at high densities. This assumption, of course, is questionable for a large fraction of experiments concerning ultracold quantum gases. For these systems (where Migdal’s theorem is a priori not applicable), an approach based on vertex corrections seems to be more promising. Nonetheless, the present approximation is a good starting point for more sophisticated techniques. On the other hand, we shall see later that RPA captures many effects found by numerically exact Monte Carlo approach. Therefore here we focus on systems with sufficiently high particle densities.

In our RPA we compute Eq. (4),

$$\pi(i\omega) = -\frac{e^2}{m^2(i\omega)^2 V} \sum_q q^2 V_q^2 \times \frac{1}{\beta} \sum_{i\nu} \mathcal{D}^{\text{RPA}}(q, i\nu) [\chi^{(0)}(q, i\omega + i\nu) - \chi^{(0)}(q, i\nu)], \quad (15)$$

using the approximated phonon Green’s function \mathcal{D}^{RPA} given by

$$\mathcal{D}^{\text{RPA}}(q, i\nu) = \frac{\mathcal{D}^{(0)}(q, i\nu)}{1 - V_q^2 \mathcal{D}^{(0)}(q, i\nu) \chi^{(0)}(q, i\nu)}. \quad (16)$$

The corresponding diagrammatic representation of the screened phonon propagator is depicted in Fig. 4. Due

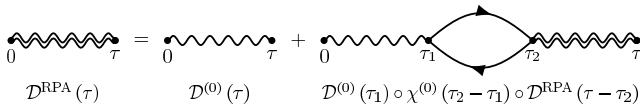


FIG. 4. Screened electron-phonon interaction: Dyson-like equation of the phonon propagator in the random phase approximation.

to the more involved structure of \mathcal{D}^{RPA} , the Matsubara summation with respect to $i\nu$ is not simple anymore. Therefore, it is more suitable to use the Lehmann representation of the Green’s functions to get rid of the fre-

quency summation. Then one obtains,¹²

$$\pi(i\omega) = -\frac{e^2}{m^2(i\omega)^2 V} \sum_q q^2 V_q^2 \int \frac{dE}{2\pi} n_{\text{B}}(E) \times \left\{ 2\text{Im} [\mathcal{D}^{\text{RPA},R}(q, E)] \chi^{(0)}(q, i\omega + E) + 2\text{Im} [\chi^{(0),R}(q, E)] \mathcal{D}^{\text{RPA}}(q, E - i\omega) - 2\text{Im} [\mathcal{D}^{\text{RPA}}(q, E) \chi^{(0)}(q, E)]^R \right\} \quad (17)$$

where the superscript R denotes the retarded component of the corresponding Green’s functions. Again, we are only interested in the real part of the conductivity, hence, the last expression in Eq. (17) can be neglected. Because of the simple structure of the free polarization loop, the remaining integral can be performed yielding

$$\text{Re}[\sigma(\omega)] = -\frac{e^2}{m^2 V^2 \omega^3} \sum_{s=\pm} \sum_{k,q} s q^2 V_q^2 n_{\text{F}}(\epsilon_k) \times \text{Im} [\mathcal{D}^{\text{RPA},R}(q, s\epsilon_{k+sq} - s\epsilon_k - \omega)] \times [n_{\text{B}}(s\epsilon_{k+sq} - s\epsilon_k - \omega) - n_{\text{B}}(s\epsilon_{k+sq} - s\epsilon_k)]. \quad (18)$$

We restrict the calculation to the zero temperature case. In this situation the polarization diagram possesses a closed analytical expression,

$$\chi(q, i\nu) = -\frac{2m}{q} \frac{1}{2\pi} \sum_{\pm} \tanh^{-1} \left(\frac{2\sqrt{2\mu m} q}{q^2 \pm 2i\nu m} \right). \quad (19)$$

This allows for an efficient calculation of the screened phonon propagator. In the case of finite temperature and quadratic dispersion relation for the impurities, the evaluation of the polarization loop is numerically rather involved. Figs. 5 and 6 show the conductivity for several parameter constellations.

As already seen in the perturbative calculation, Fig. 5 shows a pronounced shift of the secondary peak with changing chemical potential. The most prominent features, however, are seen for changing coupling strength, see Fig. 6. In the case of the LO phonon the positions of the maxima in the two-peak structure are consistent with the perturbative calculation and are located at $\omega = \Omega_0$ and $\omega = \Omega_0 + \mu$. In the case with linear phonon dispersion relation – for the acoustical phonons and a BEC system with linearized dispersion [panels b) and c)] the position of the secondary peak is different. In fact its location is still very sensitive to changing μ but without any perceivable shift at different λ .

Another interesting feature is the pseudogap, seen as the first minimum in the spectrum, which develops in the non-BEC case. Its width grows with coupling strength and is directly connected to the energy stored in the fully developed polaron state which has to be destroyed prior to excitation of the impurity. In the BEC case, no pseudogap formation is observed. The reason for that is, of course, not the absence of the polaron state as seen in

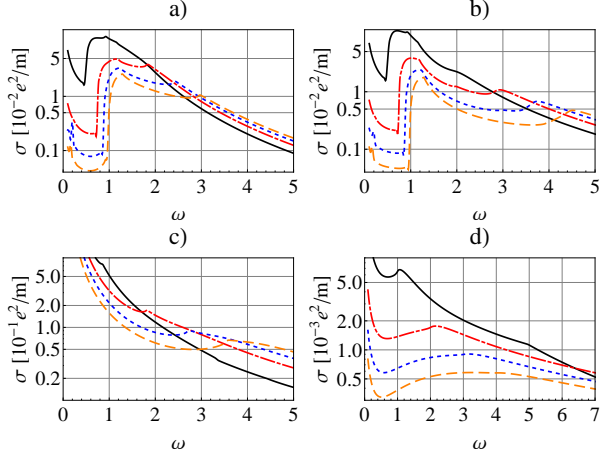


FIG. 5. (Color online) Conductance in the RPA approximation for fixed interaction strength $\lambda = 1$ and varying chemical potential $\mu = 0.5, 1, 1.5, 2$ (black solid, red dot-dashed, blue dashed and orange long-dashed line). The order of the graphs is the same as in the figures above.

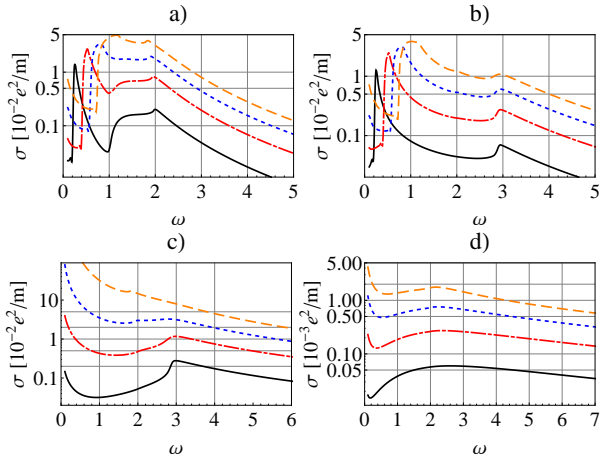


FIG. 6. (Color online) Conductance in the RPA-like approximation for fixed chemical potential $\mu = 1$ and varying interaction strength $\lambda = 0.25, 0.5, 0.75, 1$ (black solid, red dot-dashed, blue dashed and orange long-dashed line). The order of the graphs is the same as in the figures above.

the LO case. It seems that in the BEC case, due to the linearity of the bosonic dispersion, the polaron cloud is rather ‘rigid’ and the whole polaron can be excited to the higher lying fermion state (in the absorption case). On the contrary, the Drude peak tends to be enhanced.

IV. MONTE CARLO SIMULATIONS

As we have seen in the previous section, the optical spectra change considerably in the case of strongly

interacting systems. In order to corroborate the RPA results and clarify the physical picture one has to employ more advanced techniques. Quantum Monte Carlo simulation method is one of such powerful approaches which enable to access the dynamical properties of the system.^{25,26} Although in some cases it is subjected to the limitations such as finite size and the sign problem, this method has been successfully used in many polaron related problems.^{27,28} Its results have also been considered as benchmarks where exact solutions are not available.

Our Monte Carlo simulation is based on a path integral formulation of the dynamical correlation functions. We shall follow the theoretical treatment worked out in a previous work²⁹ with an extension of it to the conjugate momentum space which is convenient in our present study.

A. Formulation of path integral

For our purposes it is very convenient to reduce the phonon field to the original set of harmonic oscillator operators as $q_k = 1/\sqrt{2m_p\omega_k}(b_{-k}^\dagger + b_k)$, and $p_k = i\sqrt{m_p\omega_k/2}(b_{-k}^\dagger - b_k)$, to replace the phonon creation and annihilation operators in Hamiltonian (1), with m_p being the effective oscillator mass. So that the Fröhlich Hamiltonian is rewritten as,

$$H = \sum_q (E_q - \mu) a_q^\dagger a_q + \sum_k \left(\frac{p_k^2}{2m_p} + \frac{1}{2} m_p \omega_k^2 q_k^2 \right) + \sum_q \sum_{k \neq 0} V_k \sqrt{\frac{m_p \omega_k}{2}} (a_{q+k}^\dagger a_q q_k + \text{H.c.}). \quad (20)$$

By using the standard Trotter’s decoupling scheme, we represent the Boltzmann operator in a path integral form,

$$e^{-\beta H} \rightarrow \int \mathcal{D}x T_\tau \exp \left\{ - \int_0^\beta d\tau [h_e(\tau, x) + h_{ph}(\tau, x)] \right\} \times \prod_k |x_k(\beta)\rangle \langle x_k(0)|, \quad (21)$$

where

$$h_e(\tau, x) = \sum_q (E_q - \mu) a_q^\dagger(\tau) a_q(\tau) + \sum_q \sum_{k \neq 0} \sqrt{\frac{m_p \omega_k}{2}} [a_{q+k}^\dagger(\tau) a_q(\tau) q_k(\tau) + \text{H.c.}]$$

$$h_p(\tau, x) = \sum_k \left\{ \frac{m_p}{2} \left[\frac{\partial x_k(\tau)}{\partial \tau} \right]^2 + \frac{1}{2} m_p \omega_k^2 x_k^2(\tau) \right\}. \quad (22)$$

Here τ is imaginary time, $|x_k\rangle$ is the eigenstate of the operator q_k with eigenvalue x_k satisfying the eigen-equation $q_k|x_k\rangle = x_k|x_k\rangle$. Then we define the time evolution operator $U_x(\tau)$ along a path x as,

$$U_x(\tau) = T_\tau \exp \left\{ - \int_0^\tau d\tau' h_e[\tau', x(\tau')] \right\}. \quad (23)$$

On this path, the free energy ($\equiv F_x$) is evaluated by a trace over the fermionic part of the Boltzmann operator,

$$\begin{aligned} e^{-\beta F_x} &= e^{-\int_0^\beta d\tau h_p(x)} \text{Tr}[U_x(\beta)] \\ &= e^{-\int_0^\beta d\tau h_p(x)} \det[\mathbf{I} + \mathbf{U}_x(\beta)], \end{aligned} \quad (24)$$

where $\mathbf{U}_x(\tau)$ is the matrix representation of the time evolution operator $U_x(\tau)$. The partition function ($\equiv Z$) and total free energy is obtained by integrating out the bosonic field of x ,

$$Z = e^{-\beta F} = \int \mathcal{D}x e^{-\beta F_x}. \quad (25)$$

The expectation value of an operator O is given by

$$\langle O \rangle = \frac{1}{Z} \int \mathcal{D}x e^{-\beta F_x} \langle O \rangle_x, \quad (26)$$

where $\langle O \rangle_x$ is the average along a path x ,

$$\langle O \rangle_x = \frac{\text{Tr}[U_x(\beta)O]}{\text{Tr}[U_x(\beta)]}. \quad (27)$$

In this notation, the path integral form for the single particle Matsubara Green's function is given by:

$$\begin{aligned} G(q, \tau; q', \tau') &= \frac{1}{Z} \int \mathcal{D}x e^{-\beta F_x} G_x(q, \tau; q', \tau'), \\ G_x(q, \tau; q', \tau') &= -\langle T_\tau \hat{a}_q(\tau) \hat{a}_q^\dagger(\tau') \rangle_x, \end{aligned} \quad (28)$$

where $\hat{a}_q(\tau)$ is the Heisenberg representation of a_q , defined by

$$\hat{a}_q(\tau) = U_x^\dagger(\tau) a_q U_x(\tau). \quad (29)$$

By solving the equation of motion for the involved operators,³⁰ we get the path-dependent Green's function ($\beta \geq \tau \geq \tau' \geq 0$),

$$\begin{aligned} G_x(q, \tau; q', \tau') &= -\{ \mathbf{U}_x(\tau) [1 + \mathbf{U}_x(\beta)]^{-1} \\ &\quad \times \mathbf{U}_x^{-1}(\tau') \}_{q, q'}. \end{aligned} \quad (30)$$

The optical conductivity and absorption spectrum are derived from the current-current correlation function (8), which can be rewritten as

$$\begin{aligned} \Pi_{\mu\nu} q, \tau; q', \tau') &= \frac{1}{Z} \int \mathcal{D}x e^{-\beta F_x} \Pi_{\mu\nu, x}(q, \tau; q', \tau'), \\ \Pi_{\mu\nu, x}(q, \tau; q', \tau') &= -\frac{1}{V} \langle T_\tau \hat{j}_\mu^\dagger(q, \tau) \hat{j}_\nu(q', \tau') \rangle_x \\ &= -\frac{e^2}{m_e^2 V} \sum_{kk'} \left(k_\mu + \frac{q_\mu}{2} \right) \left(k'_\nu + \frac{q_\nu}{2} \right) \\ &\quad \times [G_x(k', \tau' + \beta; k, \tau) G_x(k + q, \tau; k' + q, \tau') \\ &\quad + G_x(k, \beta; k + q, 0) G_x(k' + q, \beta; k', 0)]. \end{aligned} \quad (31)$$

In the last line, the time-dependent Bloch-De Dominicis theorem³⁰ has been employed to decouple the many-body operators into a product of bilinear components.

B. Numerical results on dynamical responses

In our numerical calculation, the path integral is performed by the quantum Monte Carlo simulation method along with the matrix factorization and QDR decompositions in quad precision to reduce the numerical errors. During the data acquisition, the dynamical correlation function is measured after about every 100 updates and we take totally 5000-20000 samples until the simulation converges. In addition, extra 100-500 samples are swept to thermalize the starting configuration to equilibrium regime before the acquisition. After evaluating the current-current correlation function via Monte Carlo simulation, we derive the absorption spectrum $R_{\mu\nu}(q, \omega)$ by inverting the integral equation

$$\Pi_{\mu\nu}(q, \tau) = - \int_{-\infty}^{\infty} d\omega R_{\mu\nu}(q, \omega) \frac{e^{-\tau\omega}}{1 - e^{-\beta\omega}}. \quad (32)$$

From $R_{\mu\nu}(q, \omega)$, the optical conductivity is easily obtained as before by taking the following limit

$$\text{Re}[\sigma_{\mu\nu}(\omega)] = \lim_{q \rightarrow 0} \frac{\pi}{\omega} R_{\mu\nu}(q, \omega). \quad (33)$$

In order to solve the integral equation Eq. (32) for the two-particle correlation function, we have developed a renormalizing iterative fitting method. Some details of this algorithm are described in the Appendix.

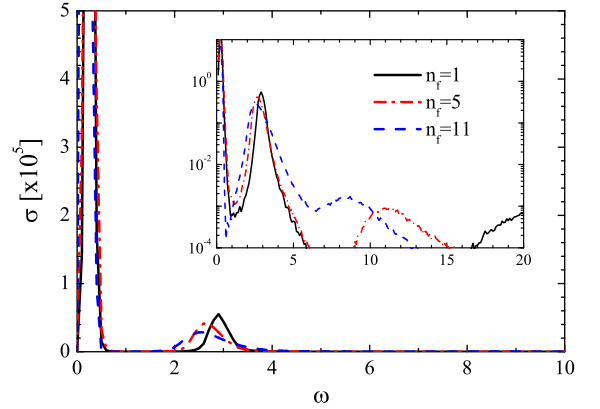


FIG. 7. (Color online) Real part of optical conductivity of a 1D conventional LO model with 25 polaronic states when $\lambda=0.5$, $\beta=10$ and $\Omega_0 = 1$. The three spectra in the main panel correspond to filling fractions: single particle (black solid), 5 (red dot-dashed) and 11 (blue dashed) particles. The inset displays the same results in semi-logarithmic scale to expose the fine structure.

In Fig. 7, we plot the real part of optical conductivity σ of Fröhlich model calculated from the quantum Monte Carlo simulation. Our simulation is performed on a 1D lattice with 25 sites with open boundary conditions. The total number of fermions ($\equiv n_f$) is adjusted between 1 and 25 by changing the chemical potential. Since we can only deal with models of finite size, here and after we confine our simulations in a momentum space of $-\pi \leq q \leq \pi$

(here measured in inverse lattice spacing), where the polaronic states are uniformly distributed. In Fig. 7, we plot the spectra for three typical cases of $n_f=1, 5$ and 11 particles. In addition to the Drude peak at $\omega=0$, the spectra show a phonon peak at $\omega=2.5\sim 3.0$ coming from the single-phonon process. In order to visualize the fine structures in the spectra, we replot these data in the inset with a semi-logarithmic scale. Here, one can clearly identify that besides the Drude and phonon peaks, there is another island of weak excitations in the spectra. This island is due to the high-order electron-phonon scattering processes and is located at the high energy part. When we increase n_f from 1, we actually introduce more polarons into the system. So that the many-body effect emerges gradually when the polarons begin to interact with each other. As a result, in the figure we observe that with n_f increase, the single-phonon peak is somewhat broadened, and the multi-phonon island is shifted towards left with an enhanced amplitude. This tendency suggests that the polaron effect can be reinforced by increasing the density of fermionic impurities.

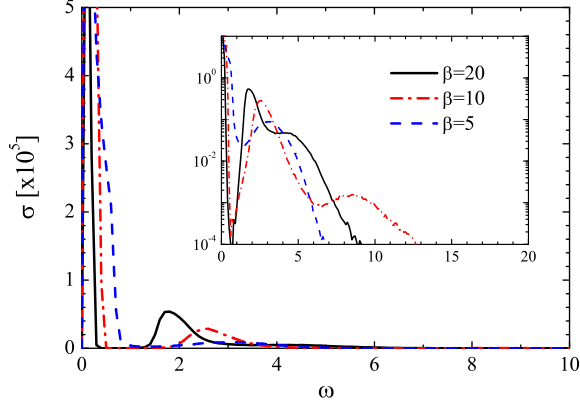


FIG. 8. (Color online) Temperature dependence of real part of optical conductivity for a 1D conventional Fröhlich model with 11 impurities on a lattice with 25 sites: $\beta=20$ (black solid), $\beta=10$ (red dot-dashed) and $\beta=5$ (blue dashed). The coupling constant is fixed to $\lambda=0.5$. The inset shows the spectra in semi-logarithmic scale.

As illustrated in Fig. 5 from RPA calculation, the single-phonon peak is located around $\omega=1.0$, that is at the frequency Ω_0 of the LO phonon. In Fig. 7, however, the single-phonon peak appears at a higher energy. This is a finite temperature effect. At $T=0$, the Fermi sea has a sharp edge at the Fermi energy E_F . Therefore, in the single-phonon process, the creation of an electron just above E_F and a hole below E_F has a sharp threshold at Ω_0 . At finite T the Fermi edge is washed out, but symmetrically both towards smaller and larger energies. On the contrary, the bosonic part is deformed in a different fashion, which leads to a perceived energy shift of the threshold for the phonon excitation. To quantify that we have performed simulations at different temperatures, see Fig. 8, adjusting β between 20 and 5. With decreasing

temperature one can see the single-phonon peak gets closer to characteristic energy of $\omega = \Omega_0$.

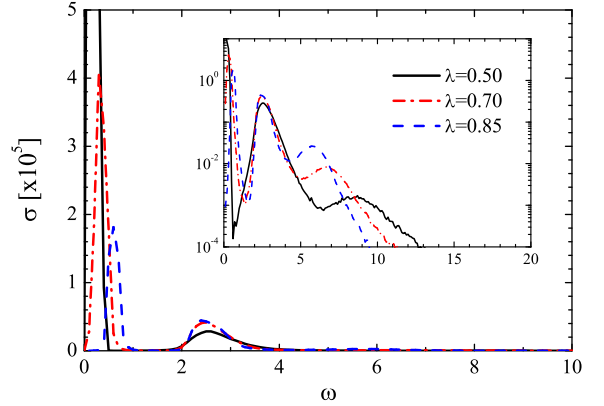


FIG. 9. (Color online) Real part of optical conductivity of a 1D conventional Fröhlich model with an LO phonon with 11 impurities on a lattice with 25 sites at $\beta=10$. The three spectra in the main frame correspond to different coupling strength λ : 0.5 (black solid), 0.7 (red dot-dashed) and 0.85 (blue dashed). The inset displays the same results in semi-logarithmic scale.

Next we investigate the dependence on the interaction strength, varying λ between 0.25 and 0.85. The last value is of the order of the band width and thus we expect it to drive the system deep into the strong coupling regime. Fig. 9 shows the results for the LO phonon situation, again on a lattice with 25 sites and 11 impurities. All curves share the general feature of a peak around $\omega \sim 2.3$, which is just the usual threshold frequency given by the phonon frequency plus the level spacing due to the finite size. This compares well with the RPA calculation. The secondary peaks due to excitation of impurities which lie deeper in the Fermi sea are much less pronounced, but undergo a shift towards lower frequencies for growing λ . This is much better seen in the inset of the figure.

More fundamental differences can be observed for the Drude peak. Starting with $\lambda=0.5$ it is moving towards finite energies while the spectral weight at $\omega=0$ almost completely vanishes. Thus a pseudogap opens up indicating that the system becomes ‘insulating’. This effect is fully covered by the RPA calculation and reflects the polaron binding energy.

Now we turn to the case of the BEC with the dispersion relation (2). We first study its dependence on the density of fermionic impurities. In Fig. 10, the real part of optical conductivity of a 1D 21-site system is depicted for filling fractions $n_f=1/21, 5/21$ and $11/21$, respectively. Here the coupling constant is set to $\lambda=0.25$, and the inset displays the spectra in a semi-logarithmic scale so as to amplify the fine structures. From the black curve of $n_f=1$, one can infer that $\lambda=0.25$ is already of intermediate strength because there is a clear pseudo gap at $\omega=0$. This is different from the RPA calculation. Thus we conclude that the formation of the gap requires a presence

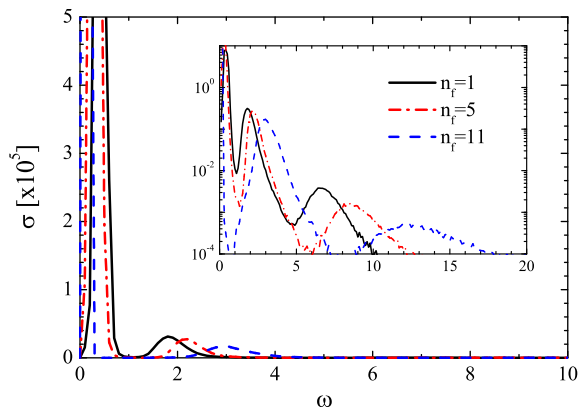


FIG. 10. (Color online) Real part of optical conductivity for a 1D system involving fermions and bosonic excitations in BEC, when $\lambda=0.25$, $\beta=10$. The three spectra in the main frame correspond to different doping levels: single (black solid), 5 (red dot-dashed) and 11 (blue dashed) fermionic impurities. The inset displays the same result in a semi-logarithmic representation.

of an additional energy scale in the system, Ω_0 in the LO case or finite level spacing in the present situation. Due to numerical restrictions we could not test out this hypothesis with sufficient precision though.

With n_f increasing to 5, one finds that the gap width and depth change, as shown by the red dot-dashed curves. If we go on increasing n_f to 11 as well as for larger fillings (not shown), as illustrated by the blue dashed curve, the gap eventually closes. Since the level spacing of an interacting system usually tends to decrease with growing number of particles this is consistent with the picture offered above.

There is also an alternative explanation for the pseudogap formation though. It might be related to the k -dependence of phonon energy $\omega_k = ck[1 + (\xi k)^2/2]^{1/2}$. As already known, the phonon modes of momenta $k = \pm 2q_F$ are responsible for the gap opening, where q_F is the Fermi momentum. When we raise up E_F , q_F and ω_{2q_F} also increase. If ω_{2q_F} is very large, these phonon states would become prohibitively difficult to generate. So that the gap will not appear. Such evolution of the gap cannot be observed in the RPA calculation, which is done for the continuum model from the outset. However, as the state-of-the-art apparatus allows for generation of rather short optical lattices we believe that the pseudogap could be observed experimentally.

The above mentioned difficulty to open a gap at high n_f can be partially eliminated by increasing the coupling strength λ . The attraction between fermions and bosons produces a negative coupling energy and tends to compensate the energy gain from phonon creation processes. In the 1D system, this coupling would end up with a gap opening, provided that λ is large enough to stabilize the phonon states of $2q_F$. In Fig. 11, we examine this property from a view of optical conductivity for the BEC po-

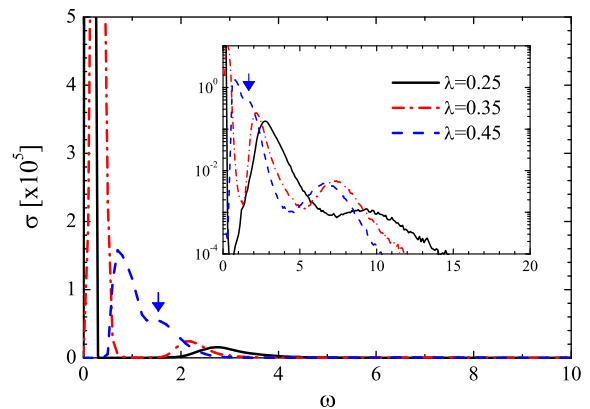


FIG. 11. (Color online) Real part of optical conductivity for a 1D model with 11 fermionic impurities in a system with 21 sites at $\beta=10$. The three spectra in the main frame correspond to different coupling strength λ : 0.25 (black solid), 0.35 (red dot-dashed) and 0.45 (blue dashed). The inset shows the same result in semi-logarithmic representation. Blue arrows in the figure indicate the phonon shoulders.

larons. We again consider 11 fermions immersed in a 1D trap of BEC with 21 sites. The gap appearance is similar to that in Fig. 9. Here $\lambda=0.25$ (black solid), 0.35 (red dot-dashed) and 0.45 (blue dashed) correspond to weak, intermediate and strong couplings, respectively. However, in Fig. 11, the phonon peak is highly modified not only in its shape but also in its position. When $\lambda=1.5$, the phonon peak even plunges into the Drude peak, giving rise to a broad shoulder. This phonon shoulder is denoted with an arrow in the main graph as well as in the inset. Such a strong delocalization effect on the phonon peak is absent in the conventional Fröhlich model. It can be attributed to the k -dependence of coupling V_k in the BEC polaron model. The most important features of the spectra are concentrated around a few k values. Since $V_k = \lambda[(\xi k)^2 / ((\xi k)^2 + 2)]^{1/4}$, if λ increases to a larger value λ' , we can find a smaller k to keep V_k invariant, i.e. $V_{k'}(\lambda') = V_k(\lambda)$, thus applying a ‘discrete’ version of renormalization transformation. That means we can attain roughly the same coupling energy by enhancing λ and reducing k together. Therefore, the phonon excitations gradually concentrate to the small k regime, and the low energy phonon modes become more favorable as λ increases. This displacement of phonon peak leads us to conclude that for large coupling, those phonon modes of small momenta or long wavelengths play more important roles in the dynamical response of the system.

V. DISCUSSION AND CONCLUSIONS

We have analyzed the spectrum of the correlation function of particle currents in a number of interacting mixtures of bosons and fermions. We considered different kinds of couplings and dispersion relations for the con-

stituent subsystems, which model electrons in semiconductors coupled to LO phonons, acoustical phonons as well as fermionic impurities which are immersed into a BEC and which interact with Bogolyubov modes of the condensate. While for the solid state realizations the quantity we calculate is the optical response, in the BEC case the correlation function of currents gives a direct access to the Bragg spectra of impurities.

While in the weak coupling case we recover all of the known physics, we find distinct effects in the strongly interacting case. Especially a pseudogap (with respect to particle-hole pair excitation) formation could be found using both the RPA approach as well as Monte Carlo simulations in 1D. We speculate that this effect is due to the finite energy stored in the polaron state, which is released/absorbed during the fermion excitation process. Remarkably, this is pertinent only to solid state realizations with an LO phonon and BEC systems of a finite size. Large BEC systems does not show up such behaviour due to linearity of their bosonic spectra in the low- k sector. Therefore in this regime the energy absorbing/emitting process occurs in such systems *without* polaron destruction.

Our approaches allow for an extension to a number of realistic experimental setups. We expect that the effects we predict could, for example, be investigated in binary systems which are similar to those used in Refs. [31] or [32].

ACKNOWLEDGMENTS

The authors thank Tobias Schuster, Raphael Scelle and Markus Oberthaler for many inspiring discussions. Financial support was provided by the DFG under Grant No. KO 2235/3 and by the ‘Enable Fund’, the CQD and the HGSFP of the University of Heidelberg.

Appendix A: Analytic continuation of two-particle Green’s function

In order to calculate the optical conductivity, we have to derive the absorption spectrum $R_{\mu\nu}(q, \omega)$ from the integral equation

$$\Pi_{\mu\nu}(q, \tau) = - \int_{-\infty}^{\infty} d\omega R_{\mu\nu}(q, \omega) \frac{e^{-\tau\omega}}{1 - e^{-\beta\omega}}, \quad (\text{A1})$$

which is called analytic continuation. In our numerical calculation, we use a renormalization iterative fitting method to do this. The original iterative fitting method is developed for the one-body Green’s function of electron²⁹. It relies on the sum-rule of electronic spectrum, which conserves the total spectral weight through the iteration process. However, for the two-body spectra like absorption spectrum $R_{\mu\nu}(q, \omega)$, there is no such a rule that conserves the total spectral sum like that of electron, except for the following properties,

$$\omega R_{\mu\nu}(q, \omega) \geq 0, \quad (\text{A2})$$

$$R_{\mu\nu}(q, -\omega) = -R_{\mu\nu}(q, \omega). \quad (\text{A3})$$

Obviously, the two-body spectrum is anti-symmetric and the total sum of spectral weight should be zero,

$$\int_{-\infty}^{\infty} d\omega R_{\mu\nu}(q, \omega) = 0. \quad (\text{A4})$$

Therefore, the standard iterative fitting method does not work here.

Nonetheless, because the spectrum is anti-symmetric, we confine our calculation in the region $0 < \omega < \infty$. We also introduce a modified spectral function

$$\tilde{R}_{\mu\nu}(q, \omega) = -\frac{R_{\mu\nu}(q, \omega)}{\Pi_{\mu\nu}(q, \beta)} \coth\left(\frac{\beta\omega}{2}\right). \quad (\text{A5})$$

Because of the anti-symmetry of $R_{\mu\nu}(q, \omega)$, on substituting $\tilde{R}_{\mu\nu}(q, \omega)$ in Eq. (A1), we can rewrite the integral equation into

$$\begin{aligned} \Pi_{\mu\nu}(q, \tau) = & - \int_0^{\infty} d\omega \tilde{R}_{\mu\nu}(q, \omega) \cosh^{-1}\left(\frac{\beta\omega}{2}\right) \\ & \times \cosh\left(\frac{\beta - \tau}{2}\omega\right) \Pi_{\mu\nu}(q, \beta). \end{aligned} \quad (\text{A6})$$

Here $\tilde{R}_{\mu\nu}(q, \omega)$ is just a renormalized form of the original spectral function, but it is easy to see this new function is positive for $\omega > 0$, and it satisfies a sum rule

$$\int_0^{\infty} d\omega \tilde{R}_{\mu\nu}(q, \omega) = 1, \quad (\text{A7})$$

which allows us to solve the integral equation of Eq. (A6) with the iterative fitting algorithm in the regime $0 < \omega < \infty$. Once $\tilde{R}_{\mu\nu}(q, \omega)$ is obtained, the original spectral function $R_{\mu\nu}(q, \omega)$ can be reproduced from Eq. (A5).

* These two authors contributed equally to this work.

¹ A. G. Truscott, K. E. Strecker, W. I. McAlexander, G. B. Partridge, and R. G. Hulet, *Science* **291**, 2570 (2001).

² G. Modugno, G. Roati, F. Riboli, F. Ferlaino, R. J. Brecha, and M. Inguscio, *Science* **297**, 2240 (2002).

³ H. Fröhlich, *Advances in Physics* **3**, 325 (1954).

⁴ L. D. Landau and S. I. Pekar, *Zh. Eksp. Teor. Fiz.* **18** (1948).

⁵ R. P. Feynman, *Phys. Rev.* **97**, 660 (1955).

⁶ J. Tempere, W. Casteels, M. K. Oberthaler, S. Knoop, E. Timmermans, and J. T. Devreese, *Phys. Rev. B* **80**, 184504 (2009).

⁷ G. L. Goodvin, A. S. Mishchenko, and M. Berciu, *Phys. Rev. Lett.* **107**, 076403 (2011).

⁸ M. Hohenadler, D. Neuber, W. von der Linden, G. Wellein, J. Loos, and H. Fehske, *Phys. Rev. B* **71**, 245111 (2005).

- ⁹ I. Bloch, J. Dalibard, and W. Zwerger, *Rev. Mod. Phys.* **80**, 885 (2008).
- ¹⁰ H. P. Büchler, P. Zoller, and W. Zwerger, *Phys. Rev. Lett.* **93**, 080401 (2004).
- ¹¹ J. Stenger, S. Inouye, A. P. Chikkatur, D. M. Stamper-Kurn, D. E. Pritchard, and W. Ketterle, *Phys. Rev. Lett.* **82**, 4569 (1999).
- ¹² G. D. Mahan, *Many-Particle Physics*, Physics of Solids and Liquids (Plenum Press, 1990).
- ¹³ J. J. Hopfield, *Phys. Rev.* **139**, A419 (1965).
- ¹⁴ H. Bruus and K. Flensberg, *Many-Body Quantum Theory in Condensed Matter Physics: An Introduction*, Oxford graduate texts in mathematics (Oxford University Press, USA, 2004).
- ¹⁵ J. T. Devreese and A. S. Alexandrov, *Reports on Progress in Physics* **72**, 066501 (2009).
- ¹⁶ M. Bruderer, A. Klein, S. R. Clark, and D. Jaksch, *Phys. Rev. A* **76**, 011605 (2007).
- ¹⁷ A. Novikov and M. Ovchinnikov, *J. Phys. B* **43**, 105301 (2010).
- ¹⁸ W. Casteels, J. Tempere, and J. T. Devreese, *Phys. Rev. A* **83**, 033631 (2011).
- ¹⁹ W. Casteels, J. Tempere, and J. T. Devreese, *Phys. Rev. A* **84**, 063612 (2011).
- ²⁰ W. Casteels, T. Van Cauteren, J. Tempere, and J. Devreese, *Laser Physics* **21**, 1480 (2011).
- ²¹ W. Casteels, J. Tempere, and J. Devreese, *Journal of Low Temperature Physics* **162**, 266 (2011).
- ²² C. J. M. Mathy, M. B. Zvonarev, and E. Demler, *Nat Phys* **8**, 881 (2012).
- ²³ A. S. Mishchenko and N. Nagaosa, in *Polarons in Advanced Materials*, Springer Series in Materials Science, Vol. 103, edited by A. S. Alexandrov (Springer Netherlands, 2007) pp. 503–544.
- ²⁴ D. Dasenbrook and A. Komnik, arXiv:1210.1466 (2012).
- ²⁵ G. De Filippis, V. Cataudella, A. S. Mishchenko, and N. Nagaosa, *Phys. Rev. B* **85**, 094302 (2012).
- ²⁶ A. S. Mishchenko, N. Nagaosa, N. V. Prokof'ev, A. Sakamoto, and B. V. Svistunov, *Phys. Rev. Lett.* **91**, 236401 (2003).
- ²⁷ A. S. Mishchenko and N. Nagaosa, *Phys. Rev. Lett.* **93**, 036402 (2004).
- ²⁸ M. Hohenadler, F. F. Assaad, and H. Fehske, *Phys. Rev. Lett.* **109**, 116407 (2012).
- ²⁹ K. Ji, H. Zheng, and K. Nasu, *Phys. Rev. B* **70**, 085110 (2004).
- ³⁰ N. Tomita and K. Nasu, *Phys. Rev. B* **56**, 3779 (1997).
- ³¹ A. Schirotzek, C.-H. Wu, A. Sommer, and M. W. Zwierlein, *Phys. Rev. Lett.* **102**, 230402 (2009).
- ³² T. Schuster, R. Scelle, A. Trautmann, S. Knoop, M. K. Oberthaler, M. M. Haverhals, M. R. Goosen, S. J. J. M. F. Kokkelmans, and E. Tiemann, *Phys. Rev. A* **85**, 042721 (2012).